Fully nonlinear hydroelastic modeling and analytic solution of large-scale floating photovoltaics in waves

Xu, Pengpeng; Wellens, Peter R.

DOI
10.1016/j.jfluidstructs.2021.103446

Publication date
2022

Document Version
Final published version

Published in
Journal of Fluids and Structures

Journal of Fluids and Structures 109 (2022) 103446

Contents lists available at ScienceDirect

Journal of Fluids and Structures

journal homepage: www.elsevier.com/locate/jfs

Fully nonlinear hydroelastic modeling and analytic solution of large-scale floating photovoltaics in waves

Pengpeng Xu, Peter R. Wellens *

Maritime and Transport Technology Department, Delft University of Technology, Leeghwaterstraat 17, Delft, 2628 CA, The Netherlands

ARTICLE INFO

Article history:
Received 14 July 2021
Received in revised form 30 September 2021
Accepted 12 November 2021
Available online xxxx

Keywords:
Large-scale floating photovoltaics
Fluid–structure interaction
Euler Bernoulli–von Kármán Beam
Stokes Waves
Third-order solution

ABSTRACT

This paper concerns the fully nonlinear fluid–structure interaction (FSI) of Large-scale floating photovoltaics (LFPV) in waves. The Euler Bernoulli–von Kármán beam models the structure while potential flow represents the fluid. A set of coupled dynamical equations is established. The fully analytic solution is sought with the unified Stokes perturbation method. The characteristic equation is derived up to third order, which has not been reported in literature before. The expressions obtained from the solution are applied to two typical cases of a pontoon LFPV and a membrane LFPV, with physical parameters from literature. The comparison with literature demonstrates our methodology for the membrane-type in waters of arbitrary depth and pontoon-type in relatively deep waters.

1. Introduction

Large-scale floating photovoltaics (LFPV) are now creating a creative solution to clean and cost-effective renewable energy production and a heavy strain on land usage (Cazzaniga et al., 2018; Soukissian et al., 2021). LFPV's nonlinear hydroelastical properties are critical to the safety and reliability of offshore solar farms, but seldom studied.

LFPV's supporting structures come in four categories: semi-submerged-type, assembled-type, pontoon-type, and membrane-type. For all the designs above, mitigating the wave load is the foremost consideration in the offshore environment (Ikhennicheu et al., 2021). The first kind of supporting device can be seen as a scaled-down semi-submersible platform (see Rosa-Clot and Tina, 2018, for more detail). The second kind of flotation structure includes many geometrical configurations and thus can only be roughly grouped according to machinery shape, which is reviewed by Oliveira-Pinto and Stokkermans (2020). Both of the last two kinds provide large flat platforms for the installation of the PV array. The fourth category, see Fig. 1 and Bjørneklett (2018) for the only industrialized example, is considered superior to the third because of its lower costs and higher reliability. Hence, polymer membrane LFPV has evoked academic interest (Trapani and Millar, 2014; Pringle et al., 2017; Kumar and Kumar, 2020; Gorjian et al., 2021). Detailed introductions of different floating PV solutions and extensive comparisons of their merits and demerits are available in literature (see Trapani et al., 2013; Trapani and Redón Santafé, 2015; Sahu et al., 2016; Patil Desai Sujay et al., 2017; World Bank Group et al., 2019).

From a dynamic viewpoint, both pontoon and membrane LFPV can be modeled as a floating sheet coupling with water beneath, which is a typical fluid–structure interaction (FSI) problem. This FSI problem requires a choice of combinations of models such as: linear-structure-linear-flow, nonlinear-structure-linear-flow, linear-structure-nonlinear-flow, and nonlinear-structure-nonlinear-flow. A discussion on the choice can also be found in Peake (2001) that studied the

* Corresponding author.
E-mail address: p.r.wellens@tudelft.nl (P.R. Wellens).

https://doi.org/10.1016/j.jfluidstructs.2021.103446

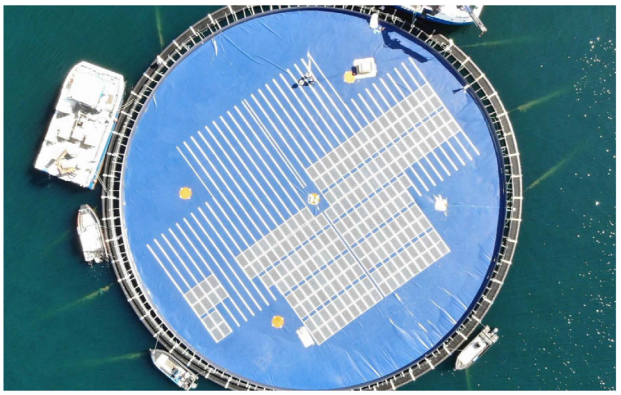

Fig. 1. Large-scale floating photovoltaics (LFPV). The large floating polymer membrane provides the foundation for photovoltaic arrays. *Source:* (Ocean Sun, 2021).

stability of a plate with mean flow loaded above. For both the pontoon and membrane LFPV, their hydroelastic models share common fundamentals with ice engineering and very large floating structures (VLFS). The Euler–Bernoulli (EB) model and linear potential flow are usually applied. Newman (1994) performed an early study near the new millennium that directly combined the equation of motion (EOM) of EB instead of starting from the "stain-stress" material mechanics.

The floating sheet problem was initially developed for the dynamics of ice sheets. Forbes (1986, 1988) analyzed the nonlinear hydroelasticity of the ice sheet in infinitely deep water. The structural nonlinearity was due to the full expression of the Gaussian curvature over the thickness. A Fourier expansion with unknown coefficients dealt with the nonlinearity. Singularities were found in the solution and explained as the breaking criterion. Balmforth and Craster (1999) investigated the reflection and transmission of surface gravity waves incident on the ice-covered ocean. The Timoshenko–Mindlin model was applied to consider the ice compression due to waves. Părău and Dias (2002) introduced geometric nonlinearity into the conventional linear ice-water model under a moving load (Squire et al., 1996) to tackle the infinite amplitude around the critical moving speed (Strathdee et al., 1991). The nonlinearity also stemmed from the Gaussian curvature; the ice's inertia was neglected. Later on, the same nonlinear model was applied to investigate waves under an ice sheet by Vanden-Broeck and Părău (2011). Porter (2019) developed a semi-analytical method applying Fourier methods and Rayleigh–Ritz methods in the modal analysis of rectangular ice sheet. The algebra-simplified system was used to investigate the scattering and propagation problems of hydroelastic waves.

Hegarty and Squire (2008) summarized and compared three widely used nonlinear plate models, i.e., Forbes, von Kármán and Drozdov: the Forbes method, as mentioned above, contains geometrical nonlinearity due to the curvature and ignores the in-plane force; the von Kármán plate linearizes the curvature and considers the in-plane force; the Drozdov model takes both nonlinearities in curvature and membrane force into account. The authors used a perturbation method to order the partial differential equations (PDE) and solve the obtained PDE with the boundary integral method.

When entering the new millennium, VLFS evoked the interest of both academia and engineering (Suzuki et al., 2006). The concept of VLFS aims to create available land for specific operations (floating airports, floating bridges, and floating storage) and general usage (artificial islands). Among numerous studies, the only full-scale test is the coastal pontoon-type Mega-Float program that used to be deployed in the Tokyo Bay for one year around the turn of the century (Lamas-Pardo et al., 2015; Suzuki et al., 2017); all of the other projects are still in the laboratory phase at most.

Wang and Meylan (2002) performed one of the earliest studies on the modeling problem of floating structures. The Euler Bernoulli (EB) beam modeled the finite-length floating plate while a linear potential wave modeled the infinite water. The numerical results were computed with a boundary element method (BEM). Later on, the linear-potential and linear-structure model was extended to circular plate in waves by Andrianov and Hermans (2003, 2005) both analytically (in unenclosed integral forms) and numerically. The von Kármán plate was introduced by Chen et al. (2003b,a). Coupled with linear wave forces, the response of nonlinear plates to multi-directional waves was studied numerically. Cheng et al. (2014, 2016a,b) combined a linear structural model and a nonlinear wave model. They investigated the time-domain FSI dynamics of VLFS edged with perforated and non-perforated plates and their combination with hybrid methods. In the theoretical part, the finite length of the structure enabled the modal expansion technique. To investigate the nonlinear influence, Cheng et al. (2017) applied the Euler Bernoulli–von Kármán (EBVK) theory in a numerical simulation utilizing a nonlinear numerical wave tank. The numerical tool was based on higher-order BEM. The research objective was to investigate the nonlinear behavior of the floating sheet when water waves traveled over a dam-shaped bathymetry. More recent studies on FSI of floating structures can be found in Ilyas et al. (2018), Liu et al. (2020), Karperaki and Belibassakis (2021a,b).

The multi-plate array is a solution to enlarge the area and decrease the vulnerability of VLFS. The theoretical model can be seen as multiple beam segments with connections in between. Riyansyah et al. (2010) optimized the connection

Table 1
Comparison of analytic models for VLFS.

FSI Model	Structure	Water
Ma et al. (2020)	First-order Linear	Second-order Nonlinear
Xu and Wellens (2021a)	Third-order Nonlinear	First-order Linear
The present article	Third-order Nonlinear	Third-order Nonlinear

design between two floating beam segments by numerical simulations. The EB beam was discretized with a finite element method (FEM), while the fluid domain was discretized with BEM. Iijima and Fujikubo (2018) studied the FSI behavior of a two-segment floating beam with a nonlinear plastic connection in both numerical (BEM+FEM) and experimental approaches. Iijima and Fujikubo (2019) analytically investigated the same model where the hydro-force was modeled as a distributed spring. Ren et al. (2019) looked into the hydrodynamic analysis of a modular floating structure and the design of connectors. The numerical models were performed with HYDROSTAR® (linear potential flow) in the fluid domain and SIMO® in the structural domain.

Besides modeling the functional structure, VLFS's nonlinear properties were also investigated by researchers. Xu and Wellens (2021b) analytically investigated the nonlinear vibration of a plate (e.g., a solar platform) subjected to static loads (e.g., hydrostatics). Three changes in the nonlinear dynamics due to statics were recognized, namely stiffening, asymmetry and softening. Yang (2017) developed an active–passive hybrid control system to limit the large nonlinear motions and deflections of the VLFS in waves. The active control was achieved by actuators in the mooring system, while the passive was provided by highly stiff connections between segments. Numerical simulations showed the better performance of the proposed control system over the existing active control. Zhang et al. (2018) came up with a network model for the floating airport (Zhang et al., 2015b), where a beam oscillator represented the runway, and discrete oscillators characterize the linear-restoring buoys. Amplitude death (see also Zhang et al., 2015a) was analyzed using the fundamental solution derived by the averaging method and calculated numerically.

From the literature, we found that fully nonlinear models suitable for LFPV's hydroelastic waves and corresponding analytic solutions are rare. The analytic solution is preferred in the early design stage of engineering. Furthermore, the simplification of deep water is inapplicable because the first solar farms are likely deployed in coastal waters. Under these considerations, two models, Ma et al. (2020) and our previous research (Xu and Wellens, 2021a), are recent additions that can be of interest. However, their FSI models are not fully nonlinear: the structural model is linear in the former, whereas the fluid model is linear in the latter. This motivates us to perform a direct continuation of our previous research, coupling the nonlinear EBVK theory with the nonlinear Stokes theory and solving the simultaneous system analytically. The analytic solution is derived up to the third order, which to our knowledge has not been reported in the literature before. The comparison between the present research and those two recent articles can be found in Table 1.

2. Mathematical model

2.1. Problem definition

The elastic deformation on the membrane of a LFPV is more significant than its motion as a whole under the same considerations as in Lamas-Pardo et al. (2015). Therefore, we restrict ourselves to hydroelastic waves with the following assumptions.

- Neglect the motion of LFPV as a whole.
  A LFPV is subjected to wave, current and wind loads and held in place by mooring. However, the influence of the global motion on the hydroelastic waves is small and negligible. Readers are referred to Ikhennicheu et al. (2021) for analytical methodologies of calculating the three kinds of load and designing the mooring system.
- Neglect all the attachments.
  The PV panels may add local mass onto the membrane. The fastenings of the PV panels may affect local stresses in the membrane. And marine growth on the bottom side of the membrane may influence the friction between fluid and membrane. However, these effects are considered small enough in our model not to affect the fundamental mechanism of hydroelastic wave propagation through the structure.
- Neglect the boundary conditions of the upstream and downstream.
  Offshore solar farms are deployed in coastal areas for reliability and maintainability. Waves in such waters are much shorter than the size of the structure. In the interior, the wave propagation is hardly affected by boundary conditions. This justifies the assumption of an infinite domain for the hydroelastic LFPV system. Similar infinite domains are also argued by Kagemoto et al. (1997, 1998), Andrianov and Hermans (2003), Batyaev and Khabakhpasheva (2015), Ma et al. (2020).

Based on the assumptions above, a mathematical model is abstracted from the engineering problem in the vertical dimension and one horizontal dimension (2D), with a beam of infinite length floating on the free surface of water without horizontal confines (see Fig. 2). The LFPV can be modeled as a nonlinear EBVK beam that considers the membrane force, while the water can be modeled by potential flow. FSI takes place as structural deformations propagate as waves through the structure.

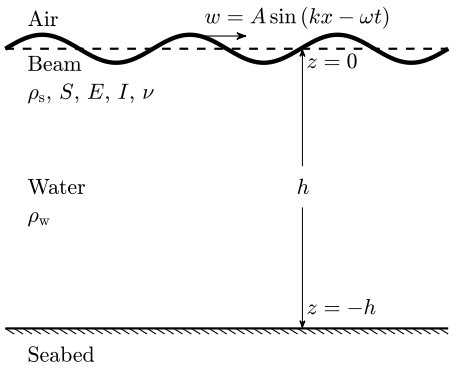

Fig. 2. The 2D sketch of hydroelastic waves in LFPV that floats on the sea surface. The structure is modeled by an EBVK beam, moving together with the water.

2.2. Nonlinear Euler Bernoulli–von Kármán theory for beam

The EBVK model is described by the material density ρ_s, Young's modulus E, Poisson's ratio ν, the rectangular cross-section $S = b\delta$ and the inertial moment $I = \frac{b\delta^3}{12(1-\nu^2)}$. Here, δ stands for the beam thickness (in z-direction) and b for the beam width (in y-direction). Under the external (hydrodynamic) load, the EOM reads

$$\rho_s S\frac{\partial^2 w}{\partial t^2} + EI\frac{\partial^4 w}{\partial x^4} - \frac{3}{2}SE\left(\frac{\partial w}{\partial x}\right)^2\frac{\partial^2 w}{\partial x^2} = q_w, \tag{1}$$

where $w(x, t)$ is the transverse displacement (in z-direction). The external excitation $q_w(x, t)$ has unit $\left[\mathrm{N\,m^{-1}}\right]$ because it is a force per unit length of the beam.

2.3. Potential theory for water

The water has density ρ_w and a uniform depth of h. Velocity potential $\phi(x, z, t)$ describes the inviscid, irrotational and incompressible flow as

$$\frac{\partial^2\phi}{\partial x^2} + \frac{\partial^2\phi}{\partial z^2} = 0. \tag{2}$$

The seabed is impenetrable:

$$\frac{\partial\phi}{\partial z} = 0 \quad \text{at} \quad z = -h. \tag{3}$$

At the free surface, the nonlinear kinematic boundary condition is

$$\frac{\partial\eta}{\partial t} + \frac{\partial\phi}{\partial x}\frac{\partial\eta}{\partial x} - \frac{\partial\phi}{\partial z} = 0 \quad \text{at} \quad z = \eta, \tag{4}$$

where $\eta(x, t)$ is the free surface elevation. The dynamic boundary condition reads

$$p + \rho_w\frac{\partial\phi}{\partial t} + \frac{\rho_w}{2}\left(\left(\frac{\partial\phi}{\partial x}\right)^2 + \left(\frac{\partial\phi}{\partial z}\right)^2\right) + \rho_w g\eta = 0 \quad \text{at} \quad z = \eta, \tag{5}$$

where $p(x, t)$ is the water pressure with unit $\left[\mathrm{N\,m^{-2}}\right]$ and $g = 9.81\left[\mathrm{m\,s^{-2}}\right]$ is the acceleration of gravity.

2.4. FSI conditions

The beam and water are coupled through the interface boundary conditions:

$$w = \eta \quad \text{and} \quad q_w = pb. \tag{6}$$

Note that the dynamic condition calculates q_w by multiplying the hydrodynamic pressure p with beam width b.

Now the structure and fluid equations are coupled at the free surface:

$$\frac{\partial w}{\partial t} + \frac{\partial\phi}{\partial x}\frac{\partial w}{\partial x} - \frac{\partial\phi}{\partial z} = 0 \tag{7}$$

and

$$\rho_s\delta\frac{\partial^2 w}{\partial t^2}+\frac{E\delta^3}{12\left(1-\nu^2\right)}\frac{\partial^4 w}{\partial x^4}-\frac{3E\delta}{2}\left(\frac{\partial w}{\partial x}\right)^2\frac{\partial^2 w}{\partial x^2}+\rho_w\frac{\partial\phi}{\partial t}+\frac{\rho_w}{2}\left(\left(\frac{\partial\phi}{\partial x}\right)^2+\left(\frac{\partial\phi}{\partial z}\right)^2\right)+\rho_w g w=0. \tag{8}$$

Here, S, I and η have been replaced or eliminated by $S=b\delta$, $I=\frac{b\delta^3}{12\left(1-\nu^2\right)}$ and Eq. (6).

After introducing normalized variables

$$\kappa=\frac{\delta^2 E}{12\rho_s\left(1-\nu^2\right)},\quad \alpha=\frac{3E}{2\rho_s}\quad\text{and}\quad \beta=\frac{\rho_w}{\rho_s\delta}, \tag{9}$$

the dynamic interface condition Eq. (8) becomes

$$\frac{\partial^2 w}{\partial t^2}+\kappa\frac{\partial^4 w}{\partial x^4}-\alpha\left(\frac{\partial w}{\partial x}\right)^2\frac{\partial^2 w}{\partial x^2}+\beta\frac{\partial\phi}{\partial t}+\frac{\beta}{2}\left(\left(\frac{\partial\phi}{\partial x}\right)^2+\left(\frac{\partial\phi}{\partial z}\right)^2\right)+\beta g w=0\quad\text{at}\quad z=w. \tag{10}$$

3. Methodology

3.1. Perturbation

For water waves, the wave steepness ak, or the wave slope equivalently, is a small parameter that can scale their nonlinear behavior (Stokes, 2009; Levi-Civita, 1925; Struik, 1926; Ursell, 1953; Schwartz, 1974; Holthuijsen, 2007). For the hydroelastics of an EBVK beam, our previous study (Xu and Wellens, 2021a) has shown that the nonlinear stiffness is two orders higher than the linear stiffness, which is briefly summarized in Appendix A. Therefore, we introduce the wave steepness as the perturbation

$$\varepsilon=Ak. \tag{11}$$

The nonlinear potential in free surface conditions can be expanded into a series form in terms of the wave steepness (Ak, A^2k^2, A^3k^3, $\cdots$). This perturbation is used to expand the independent time variable t (see Section 3.2), the structural deformation $w\left(x,t\right)$ and the velocity potential $\phi\left(x,z,t\right)$ (see Section 3.3).

3.2. Time expansion

A new time-scale τ is introduced by the transformation

$$\tau\sim t\left(1+\varepsilon^2\Omega+\mathcal{O}\left(\varepsilon^4\right)\right). \tag{12}$$

Notice that the series of the time coordinate is equivalent to the procedure for the frequency change

$$\omega\sim\omega_1\left(1+\varepsilon^2\Omega+\mathcal{O}\left(\varepsilon^4\right)\right). \tag{13}$$

The fundamental idea of the expansion method of Eqs. (12) and (13) was initially brought forward by Stokes, and is known as the Lindstedt–Poincaré Method nowadays. The reason why we use ε^2 instead of ε^1 in Eq. (13) is that secular terms occur at the third order in both the structure and fluid domain (see Section 4.3). Even if we add a term in $\mathcal{O}\left(\varepsilon^1\right)$ in Eqs. (12) and (13), the added term will turn out to be zero while deriving the second-order solution.

The partial derivatives about time t are also expanded according to Eq. (12):

$$\frac{\partial}{\partial t}\sim\left(1+\varepsilon^2\Omega+\mathcal{O}\left(\varepsilon^4\right)\right)\frac{\partial}{\partial\tau}\quad\text{and}\quad\frac{\partial^2}{\partial t^2}\sim\left(1+2\varepsilon^2\Omega+\mathcal{O}\left(\varepsilon^4\right)\right)\frac{\partial^2}{\partial\tau^2}. \tag{14}$$

Now the kinematic and dynamic conditions Eqs. (7) and (10) become

$$\left(1+\varepsilon^2\Omega\right)\frac{\partial w}{\partial\tau}+\frac{\partial w}{\partial x}\left.\frac{\partial\phi}{\partial x}\right|_{z=w}-\left.\frac{\partial\phi}{\partial z}\right|_{z=w}=0 \tag{15}$$

and

$$\begin{aligned}\left(1+2\varepsilon^2\Omega\right)\frac{\partial^2 w}{\partial\tau^2}+\kappa\frac{\partial^4 w}{\partial x^4}-\alpha\left(\frac{\partial w}{\partial x}\right)^2\frac{\partial^2 w}{\partial x^2}+\beta\left(1+\varepsilon^2\Omega\right)\left.\frac{\partial\phi}{\partial\tau}\right|_{z=w}\\+\frac{\beta}{2}\left(\left(\left.\frac{\partial\phi}{\partial x}\right|_{z=w}\right)^2+\left(\left.\frac{\partial\phi}{\partial z}\right|_{z=w}\right)^2\right)+\beta g w=0.\end{aligned} \tag{16}$$

3.3. Solution expansion

The structural deformation in the proposed FSI model is expanded in terms of ε in the same manner of Stokes' wave theory (see also Ma et al., 2020; Xu and Wellens, 2021a):

$$w \sim \varepsilon^1 w_1 + \varepsilon^2 w_2 + \varepsilon^3 w_3 + \cdots = w_\mathrm{l} + w_\mathrm{q} + w_\mathrm{c} + \cdots , \tag{17}$$

where the subscripts l, q and c indicate linear, quadratic and cubic, respectively.

The velocity potential in the water below the surface is also expanded like Eq. (17):

$$\phi \sim \varepsilon^1 \phi_1 + \varepsilon^2 \phi_2 + \varepsilon^3 \phi_3 + \cdots = \phi_\mathrm{l} + \phi_\mathrm{q} + \phi_\mathrm{c} + \cdots \quad \text{for} \quad -h \leqslant z \leqslant 0. \tag{18}$$

At the free surface $z = w$, the velocity potential is expanded utilizing the Stokes expansion. The Stokes expansion is an application of the Taylor expansion around $z = 0$ considering a small transverse displacement w

$$\phi|_{z=w} = \phi|_{z=0} + \frac{w^1}{1!}\left.\frac{\partial^1 \phi}{\partial z^1}\right|_{z=0} + \frac{w^2}{2!}\left.\frac{\partial^2 \phi}{\partial z^2}\right|_{z=0} + \cdots . \tag{19}$$

Substitution of Eqs. (17) and (18) into Eq. (19) yields

$$\phi|_{z=w} = \varepsilon^1 \phi_1 + \varepsilon^2 \left(\phi_2 + w_1 \frac{\partial \phi_1}{\partial z}\right) + \varepsilon^3 \left(\phi_3 + w_1 \frac{\partial \phi_2}{\partial z} + w_2 \frac{\partial \phi_1}{\partial z} + \frac{w_1^2}{2}\frac{\partial^2 \phi_1}{\partial z^2}\right) + \mathcal{O}\left(\varepsilon^4\right). \tag{20}$$

And all the partial derivatives $\frac{\partial \phi}{\partial}\big|_{z=w}$ are expanded with the Stokes expansion, too.

In this article, we refer to our solution methodology as the unified Stokes perturbation method because the mathematical treatments to perturb and expand the PDE originate from Stokes (see also Section 3.2). Notice that all the ϕ-associated terms on the right-hand side of Eq. (20) are evaluated at $z = 0$. Hereafter, we omit the "evaluate-at-zero" symbol in the two interface boundary conditions for brevity.

3.4. Hierarchic partial differential equations

We substitute Eq. (18) into Eqs. (2) and (3), and substitute Eqs. (17) and (20) into Eqs. (15) and (16). Then terms are collected and sorted according to the rational power of the perturbation ε and retained up to the third order. After these manipulations, we obtain a series of hierarchic PDEs.

- $\mathcal{O}\left(\varepsilon^1\right)$:

$$\frac{\partial^2 \phi_\mathrm{l}}{\partial x^2} + \frac{\partial^2 \phi_\mathrm{l}}{\partial z^2} = 0 \tag{21}$$

$$\left.\frac{\partial \phi_\mathrm{l}}{\partial z}\right|_{z=-h} = 0 \tag{22}$$

$$\frac{\partial w_\mathrm{l}}{\partial \tau} - \frac{\partial \phi_\mathrm{l}}{\partial z} = 0 \tag{23}$$

$$\frac{\partial^2 w_\mathrm{l}}{\partial \tau^2} + \kappa \frac{\partial^4 w_\mathrm{l}}{\partial x^4} + \beta \mathrm{g} w_\mathrm{l} + \beta \frac{\partial \phi_\mathrm{l}}{\partial \tau} = 0 \tag{24}$$

- $\mathcal{O}\left(\varepsilon^2\right)$

$$\frac{\partial^2 \phi_\mathrm{q}}{\partial x^2} + \frac{\partial^2 \phi_\mathrm{q}}{\partial z^2} = 0 \tag{25}$$

$$\left.\frac{\partial \phi_\mathrm{q}}{\partial z}\right|_{z=-h} = 0 \tag{26}$$

$$\frac{\partial w_\mathrm{q}}{\partial \tau} - \frac{\partial \phi_\mathrm{q}}{\partial z} = w_\mathrm{l} \frac{\partial^2 \phi_\mathrm{l}}{\partial z^2} - \frac{\partial w_\mathrm{l}}{\partial x}\frac{\partial \phi_\mathrm{l}}{\partial x} \tag{27}$$

$$\frac{\partial^2 w_\mathrm{q}}{\partial \tau^2} + \kappa \frac{\partial^4 w_\mathrm{q}}{\partial x^4} + \beta \mathrm{g} w_\mathrm{q} + \beta \frac{\partial \phi_\mathrm{q}}{\partial \tau} = -\beta w_\mathrm{l} \frac{\partial^2 \phi_\mathrm{l}}{\partial \tau \partial z} - \frac{\beta}{2}\left(\left(\frac{\partial \phi_\mathrm{l}}{\partial x}\right)^2 + \left(\frac{\partial \phi_\mathrm{l}}{\partial z}\right)^2\right) \tag{28}$$

- $\mathcal{O}\left(\varepsilon^3\right)$

$$\frac{\partial^2 \phi_\mathrm{c}}{\partial x^2} + \frac{\partial^2 \phi_\mathrm{c}}{\partial z^2} = 0 \tag{29}$$

$$\left.\frac{\partial \phi_c}{\partial z}\right|_{z=-h} = 0 \tag{30}$$

$$\begin{aligned}\frac{\partial w_c}{\partial \tau} - \frac{\partial \phi_c}{\partial z} =& -\Omega \frac{\partial w_l}{\partial \tau} - \frac{\partial w_l}{\partial x}\frac{\partial \phi_q}{\partial x} - \frac{\partial w_q}{\partial x}\frac{\partial \phi_l}{\partial x} \\ &+ w_l \frac{\partial^2 \phi_q}{\partial z^2} + w_q \frac{\partial^2 \phi_l}{\partial z^2} - w_l \frac{\partial w_l}{\partial x}\frac{\partial^2 \phi_l}{\partial x \partial z} + \frac{w_l^2}{2}\frac{\partial^3 \phi_l}{\partial z^3}\end{aligned} \tag{31}$$

$$\begin{aligned}\frac{\partial^2 w_c}{\partial \tau^2} + \kappa \frac{\partial^4 w_c}{\partial x^4} + \beta g w_c + \beta \frac{\partial \phi_c}{\partial \tau} =& -2\Omega \frac{\partial^2 w_l}{\partial \tau^2} - \beta \Omega \frac{\partial \phi_l}{\partial \tau} - \beta w_l \frac{\partial^2 \phi_q}{\partial \tau \partial z} - \beta w_q \frac{\partial^2 \phi_l}{\partial \tau \partial z} \\ &- \beta \frac{\partial \phi_l}{\partial x}\frac{\partial \phi_q}{\partial x} - \beta \frac{\partial \phi_l}{\partial z}\frac{\partial \phi_q}{\partial z} - \beta w_l \frac{\partial \phi_l}{\partial x}\frac{\partial^2 \phi_l}{\partial x \partial z} \\ &+ \alpha \left(\frac{\partial w_l}{\partial x}\right)^2 \frac{\partial^2 w_l}{\partial x^2} - \beta w_l \frac{\partial \phi_l}{\partial z}\frac{\partial^2 \phi_l}{\partial z^2} - \frac{\beta w_l^2}{2}\frac{\partial^3 \phi_l}{\partial \tau \partial z^2}\end{aligned} \tag{32}$$

4. Analytical solution

4.1. First-order solution

For the application of separation of variables, we define

$$\phi_l(x, z, \tau) = \varphi_l(\tau)\, \xi_1(x)\, \zeta_1(z)\,. \tag{33}$$

The substitution of Eq. (33) into Eqs. (21) and (22) provides solutions of the horizontal and vertical-space-dependent functions $\xi_1(x)$ and $\zeta_1(z)$:

$$\phi_l = \varphi_l(\tau) \cos(kx) \cosh(k(z+h))\,. \tag{34}$$

Notice that two arbitrary integral constants arise for $\xi_1(x)$ and $\zeta_1(z)$. We do not explicitly show the integral constants but merge them into the undetermined time-dependent function $\varphi_l(\tau)$.

Next, applying partial differentiation of Eq. (24) with respect to τ:

$$\frac{\partial^3 w_l}{\partial \tau^3} + \kappa \frac{\partial^5 w_l}{\partial x^4 \partial \tau} + \beta g \frac{\partial w_l}{\partial \tau} + \beta \frac{\partial^2 \phi_l}{\partial \tau^2} = 0. \tag{35}$$

One can obtain an ordinary differential equation in terms of τ by inserting Eqs. (23) and (34) into Eq. (35):

$$(k \tanh(kh) + \beta)\frac{\partial^2 \varphi_l}{\partial \tau^2} + k \tanh(kh)\left(k^4 \kappa + \beta g\right)\varphi_l = 0 \tag{36}$$

The solution of Eq. (36) is:

$$\varphi_l(\tau) = C_1 \sin(\omega_1 \tau + \theta)\,, \tag{37}$$

where

$$\omega_1 = \sqrt{\frac{k \tanh(kh)\left(k^4 \kappa + \beta g\right)}{k \tanh(kh) + \beta}}. \tag{38}$$

Here, the amplitude C_1 contains the three arbitrary integral constants for φ_l, ξ_1 and ζ_1; the arbitrary phase shift θ is omitted in the remainder of this article because it does not affect the properties of the propagating waves.

Combination of Eqs. (34) and (38) offers the general solution of ϕ_l:

$$\phi_l = C_1 \sin(kx - \omega_1 \tau) \cosh(k(z+h))\,. \tag{39}$$

Inserting Eq. (39) into Eq. (23) leads to

$$w_l = \frac{C_1 k \sinh(kh)}{\omega_1} \cos(kx - \omega_1 \tau)\,. \tag{40}$$

Then we introduce the amplitude of the first-order wave:

$$A_l = \frac{C_1 k \sinh(kh)}{\omega_1}, \tag{41}$$

by means of which Eqs. (39) and (40) can be rewritten as

$$w_l = A_l \cos(kx - \omega_1 \tau)\,, \tag{42}$$

and

$$\phi_{\mathrm{l}} = \frac{A_{\mathrm{l}}\omega_1}{k\sinh(kh)}\sin(kx-\omega_1\tau)\cosh(k(z+h)). \tag{43}$$

Eqs. (21)–(24), (42), (42), (43) and (43) demonstrate the linearity of the first-order system. The derived solution is equal to the first-order solution of Xu and Wellens (2021a).

4.2. Second-order solution

At the second and third order, the constant coefficients are too long to show here in the article. Hence, we write these coefficients in terms of c_n ($n = 1, \ldots, 12$). Their complete expressions can be found in Appendix B.

By separation of variables, one can solve the space-dependent part of ϕ_{q} using the same approach as Section 4.1

$$\phi_{\mathrm{q}} = \varphi_{\mathrm{q}}(\tau)\cos(2kx)\cosh(2k(z+h)). \tag{44}$$

Take the derivative of Eq. (28) about τ:

$$\frac{\partial^3 w_{\mathrm{q}}}{\partial\tau^3} + \kappa\frac{\partial^5 w_{\mathrm{q}}}{\partial x^4\partial\tau} + \beta g\frac{\partial w_{\mathrm{q}}}{\partial\tau} + \beta\frac{\partial^2\phi_{\mathrm{q}}}{\partial\tau^2} = -\beta\frac{\partial w_{\mathrm{l}}}{\partial\tau}\frac{\partial^2\phi_{\mathrm{l}}}{\partial\tau\partial z} - \beta w_{\mathrm{l}}\frac{\partial^3\phi_{\mathrm{l}}}{\partial\tau^2\partial z} - \beta\frac{\partial\phi_{\mathrm{l}}}{\partial x}\frac{\partial^2\phi_{\mathrm{l}}}{\partial\tau\partial x} - \beta\frac{\partial\phi_{\mathrm{l}}}{\partial z}\frac{\partial^2\phi_{\mathrm{l}}}{\partial\tau\partial z}. \tag{45}$$

Next, we insert Eq. (27) into Eq. (45) and make use of Eqs. (42)–(44). After some manipulations, we obtain

$$c_1\frac{\partial^2\varphi_{\mathrm{q}}}{\partial\tau^2} + c_2\varphi_{\mathrm{q}} = A^2c_3\sin(2kx-2\omega_1\tau). \tag{46}$$

The particular solution of Eq. (46) for the plane propagating wave is

$$\varphi_{\mathrm{q}} = A^2c_4\sin(2kx-2\omega_1\tau). \tag{47}$$

Substitution of Eq. (47) into Eq. (44) yields

$$\phi_{\mathrm{q}} = A^2c_5\cosh(2k(z+h))\sin((2kx-2\omega_1\tau)) + C_2x + C_3\tau, \tag{48}$$

where C_2 and C_3 are undetermined integral constants with dimensions of $\left[\mathrm{m\,s^{-1}}\right]$ and $\left[\mathrm{m^2\,s^{-2}}\right]$, respectively. The constant C_2 corresponds to a uniform velocity. The constant C_3 gives a contribution to the mean pressure and is therefore related to the mean free-surface level (see Dingemans, 1997). In absence of current and horizontal movement of the LFPV system

$$C_2 = 0. \tag{49}$$

The other integral constant C_3 will be determined after solving the second-order wave w_{q}.

Inserting Eq. (48) into Eq. (27) leads to

$$w_{\mathrm{q}} = A_{\mathrm{q}}\cos(2kx-2\omega_1\tau), \tag{50}$$

where the second-order amplitude is

$$A_{\mathrm{q}} = A^2c_6. \tag{51}$$

Substitution of Eqs. (42), (43), (48) and (50) into Eq. (28) determines the integral constant C_3 by equating the constant terms to zero. The result is

$$C_3 = -\frac{A^2\omega_1^2}{4\sinh^2(kh)}. \tag{52}$$

Now the second-order potential reads

$$\phi_{\mathrm{q}} = A^2c_5\cosh(2k(z+h))\sin((2kx-2\omega_1\tau)) - \frac{A^2\omega_1^2}{4\sinh^2(kh)}\tau. \tag{53}$$

Eqs. (25)–(28), (50) and (53) demonstrate that the second-order system is not related to the structural nonlinearity but only to the nonlinearity in the fluid. In other words, our nonlinear model considers only the linear EB theory up to the second-order system. The nonlinearity of EBVK will become apparent in the third order (see Section 4.3). Therefore, our theory up to second-order fundamentally models the same hydro-elastic system as Ma et al. (2020), in which a linear beam and nonlinear water waves are coupled. However, our results and those in Ma et al. (2020) differ significantly (see Section 5) because of different potential expansions.

Note that both expressions of ϕ_{q} and w_{q} can be rewritten in the form of $A^2k^2\cdot(\cdots)$, which corresponds to the second-order expansion as long as ω_1 is replaced by Eq. (38).

4.3. Third-order solution

Sections 4.1 and 4.2 have given expressions of wave and potential up to the second order. What is left unknown is the undetermined low frequency Ω and the third-order solution. This demonstrates that the nonlinear influence on the dispersion relation, i.e., the amplitude dispersion, only occurs at the third order (see Section 4.3.1). This is logically consistent with the nonlinear models of the EBVK only, and the third-order Stokes free surface waves only, too.

The procedure for obtaining the third-order solution is performed in a similar way as that for the second order in Section 4.2. However, all the mathematical expressions are too long to present here. Therefore, we do not show the complete mathematical expressions but articulate the procedure in eight steps.

Step (1): substitute Eqs. (42), (43), (50) and (53) into Eq. (31). This step is to express the unknown third-order variables with the known first-order and second-order variables.
Step (2): substitute Eqs. (42), (43), (50) and (53) into Eq. (32). This step does the same as Step (1).
Step (3): substitute Step (1) into the time derivative of Step (2). This step is to represent w_c by ϕ_c.
Step (4): collect and sort trigonometric functions of order one, two and three; avoiding secular terms requires that the coefficient of the linear harmonic is zero.
Step (5): solve the undetermined frequency Ω using Step (4). The result of this step gives the most significant nonlinearity of FSI wave propagation, i.e., amplitude dispersion.
Step (6): substitute Ω back into the equation of Setp (4); or, equivalently, eliminate all linear terms associated with $\sin(kx - \omega_1\tau)$.
Step (7): solve the third-order potential $\phi_3(x, z, \tau)$ via Step (6).
Step (8): solve the only remaining unknown, i.e., the third-order wave $w_3(x, \tau)$, via Step (1).

4.3.1. Amplitude dispersion

In Step (4) one will find that only terms that scale with $\sin(kx - \omega_1\tau)$ remain; there are no terms that scale with $\cos(kx - \omega_1\tau)$. Step (5) leads to the solution for the low frequency:

$$\varepsilon^2\Omega = \left(A^2k^2\right)\frac{c_7}{c_8} \tag{54}$$

Substitution of Eq. (54) into Eq. (13) yields the nonlinear dispersion relation. During propagating, a group of waves disperses with both frequency and amplitude. On the one hand, structural nonlinearity results in amplitude dispersion that is two orders higher than linear in the decoupled EBVK beam. On the other hand, amplitude dispersion also occurs in the third order if only Stokes waves are considered. Amplitude dispersion is an inherent feature of nonlinearity in both EBVK and the third-order Stokes. Our solution also has amplitude dispersion at the third order in the considered FSI model.

4.3.2. The third-order potential and waves

After inserting Eq. (54) into Eqs. (29)–(32), a similar procedure as in Section 4.2 – separating ϕ_c, taking the partial differentiation of Eq. (32) about τ and substituting Eq. (31) – leads to the solution of the third-order potential ϕ_c, wave w_c and amplitude A_c:

$$\phi_c = A_1^3 c_9 c_{10} \sin(3kx - 3\omega_1\tau) \tag{55}$$

and

$$w_c = A_c \cos(3kx - 3\omega_1\tau), \tag{56}$$

where

$$A_c = A_1^3 \frac{c_{11}}{c_{12}} \tag{57}$$

Note that both expressions of ϕ_c and w_c can be rewritten into the form $A^3k^3 \cdot (\cdots)$ that corresponds to the third-order expansion as long as ω_1 is replaced by Eq. (38). This is similar to the second-order solution (see Section 4.2).

5. Case study and discussion

5.1. Two cases

As reviewed in Section 1, the steel pontoon-type LFPV is modeled as a less flexible plate, whereas the polymer membrane-type LFPV is modeled as a more flexible membrane. The EBVK theory is applicable to both of these two models. We perform the case study based on information from two published articles. The first one, Ma et al. (2020), is for the plate-type and referred to as Case 1. The second one, Schreier and Jacobi (2020), is for the membrane-type and referred to as Case 2. The former is a numeric–analytic hybrid study and has been reviewed in Section 1. The latter is an experimental study that was carried out in a wave tank, investigating the hydroelastic behavior of highly flexible VLFS. Table 2 gives the physical parameters of two cases.

Table 2
Physical Parameters of Case 1 and Case 2.

Parameter	Unit	Case 1 Ma et al. (2020) Pontoon-type	Case 2 Schreier and Jacobi (2020) Membrane-type
ρ_s	$\mathrm{kg\,m^{-3}}$	600	116
δ	m	0.02	0.005
E	$\mathrm{N\,m^{-2}}$	1 641 600	560 000
ν	–	0.3	0.4
ρ_w	$\mathrm{kg\,m^{-3}}$	1000	1000
h	m	0.8	1.0
A_{max}	m	0.1	0.02
k	$\mathrm{rad\,m^{-1}}$	0.89-1.57	6.34-12.69
ω_1	$\mathrm{rad\,s^{-1}}$	2.167-4.189	7.5-14

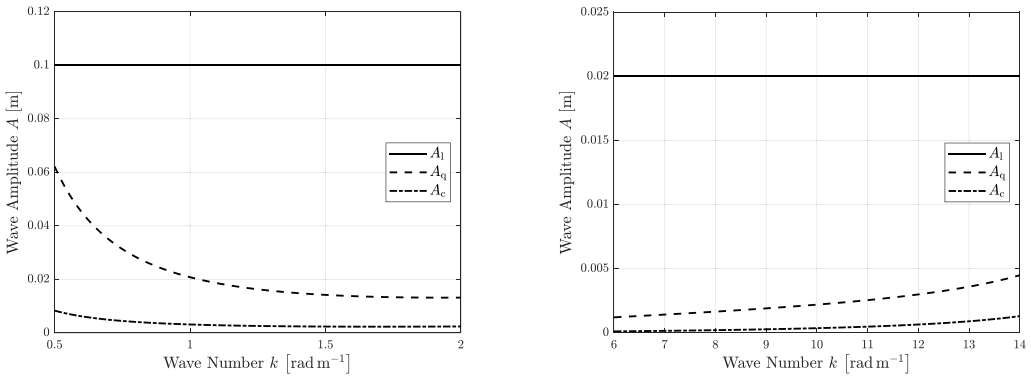

(a) Case 1 (b) Case 2

Fig. 3. Wave amplitudes varying with the wave number k in Case 1 and Case 2. The first-order amplitudes in the two cases are set to be consistent with the characteristic values in Case 1 and Case 2, respectively.

5.2. Higher order waves

5.2.1. Existence

A higher-order wave cannot exist independently, but has to be enslaved to the primary wave. This can be demonstrated by the following facts. Firstly, the higher-order amplitudes, A_q and A_c, are functions of the linear amplitude, A_l (see Eqs. (50), (51), (56) and (57)). In other words, $A_q = A_c = 0$ when $A_l = 0$. Secondly, waves including higher-order waves do not satisfy the linear dispersion relation.

5.2.2. Amplitudes

Fig. 3 shows the nonlinear amplitudes as a function of the wavenumber k given by Eqs. (51) and (57) for both cases. The first-order amplitudes are fixed. $A_l = 0.1$ and $0.5 < k < 2$ for case 1 to be consistent with the characteristic values for Case 1 (Ma et al., 2020, Fig. 6); $A_l = 0.02$ and $6 < k < 14$ for Case 2 (Schreier and Jacobi, 2020, Table 2). Fig. 4 presents the variation of the second- and third-order amplitudes in Case 1 and Case 2 with wavenumbers k and the linear amplitudes A_l.

Fig. 4 indicates that the nonlinear amplitudes are proportional to the linear amplitude, which is physically expected. The influence of wavenumber k is not identical in the different cases. In Case 1, the higher-order amplitudes are evidently larger for small wavenumbers. In Case 2, the higher-order amplitudes increase with the wavenumber, meaning the nonlinearity is pronounced for shorter waves.

The difference in k's influence can be explained by singularities in Eqs. (51) and (57). k appears in both the numerator and denominator. It is almost impossible to isolate k because of the trigonometrics and hyperbolics that are transcendental. This results in possible singularity(ies) depending on the values of the chosen physical parameters. Fig. 3(a) shows that $k = 0$ is a singularity given the parameters of Case 1. From the posterior viewpoint, the results imply that the solution is suitable for Case 2, but not fully suitable for Case 1.

The water depth h plays an important role in the nonlinear solutions. The derived solution contains singularities when approaching a zero wavenumber (the infinitely long wave) and zero water depth. The unexpected amplitude decrease for the pontoon LFPV in very shallow water is obviously affected by these singularities. Fig. 5 illustrates the nonlinear amplitude dependence on the water depth and the wavenumber. In deep water, starting from e.g., $h = 10\,\mathrm{m}$, the nonlinear amplitudes increase with the wavenumber. When the water depth $h \to 0$, a singularity occurs in both cases. In

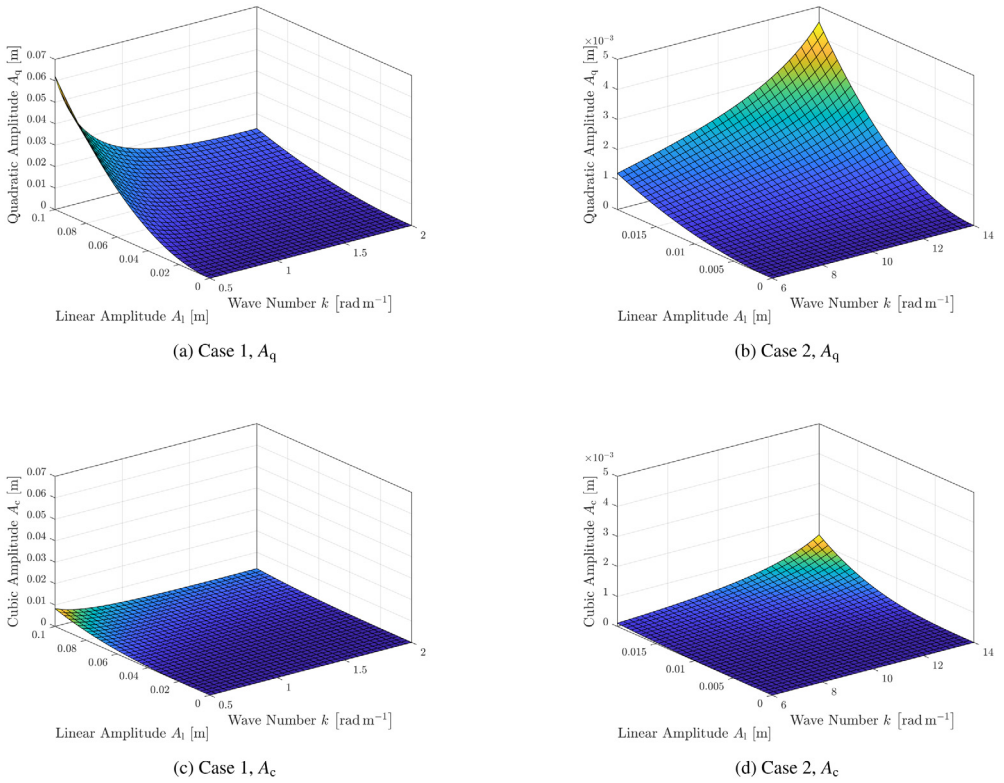

(a) Case 1, A_q (b) Case 2, A_q

(c) Case 1, A_c (d) Case 2, A_c

Fig. 4. Higher-order wave amplitudes varying with the wave number k and the linear wave amplitude A_l in Case 1 and Case 2. Ranges are roughly consistent with the characteristic values in literature.

deeper water, the nonlinear amplitudes in Case 1 are increasing with the wavenumber indeed. Therefore, the unexpected monotonic decrease in Case 1 (see Figs. 3(a), 4(a) and 4(c)) can be explained by the influence of the singularity at zero water depth. Thus, for Case 1 our analytic solution is valid for relatively deep water.

Besides the singularity at $h = 0$, exceeding a threshold steepness is also a possible reason for nonphysical the results. Case 1's Ursell number, calculated with Eq. (58) (Fenton and McKee, 1990; Fenton, 1999), is in the range of $6.2563 \leq Ur \leq 19.4688$ (according to Table 2). In free surface water waves, the Stokes expansion does not apply for the range of $Ur > 10$ neither.

$$Ur = \frac{2A\left(\frac{2\pi}{k}\right)^2}{h^3} \tag{58}$$

5.2.3. Wave forms

Fig. 6 visualizes the nonlinear wave of our solution up to the third order, using the physical parameters in Table 2. In Case 1, $k = 0.7134$ ($\omega_1 = 1.9$) and 0.8848 ($\omega_1 = 2.3$) while $A_l = 0.05$ so that $0.01 < \varepsilon < 0.1$. In Case 2, $k = 9.0$ and 11.0 while $A = 0.01$ so that $0.01 < \varepsilon < 0.1$, too. The example waves of Case 1 manifest strong nonlinearity because the higher-order amplitudes are relatively large. The nonlinear amplitudes increase with longer waves, as discussed in Section 5.2.2. In contrast, the waves in Case 2 are weakly nonlinear. The nonlinearity increases with shorter waves, as physically expected.

5.2.4. Comparison

Fig. 7 compares the analytical solutions of the present article with Ma et al. (2020) in Case 1. Fig. 7(a) compares the ratio of the quadratic amplitude A_q over the linear amplitude A_l where $A_l = 0.1\,\text{m}$. The continuous solid line represents our results, where A_l is calculated by Eq. (41) A_q by Eq. (51); the crosses are the data taken from Fig. 6 of Ma et al. (2020). Fig. 7(b) presents the time history of a particularly nonlinear wave with incident wave period $T = 2\,\text{s}$ and amplitude $A_l = 0.05\,\text{m}$. The solid line is our results, in which the total amplitude is based on Eq. (17); the crosses are the data taken from Fig. 5 of Ma et al. (2020).

Fig. 7(a) displays the most significant difference between our analytical solution and Ma et al. (2020): their solution gives unreasonably large nonlinear amplitudes in a common frequency range, but our solution does not. The distinction stems from a different treatment of the potential ϕ on the interface boundary conditions (see Eq. (19)). The change in the

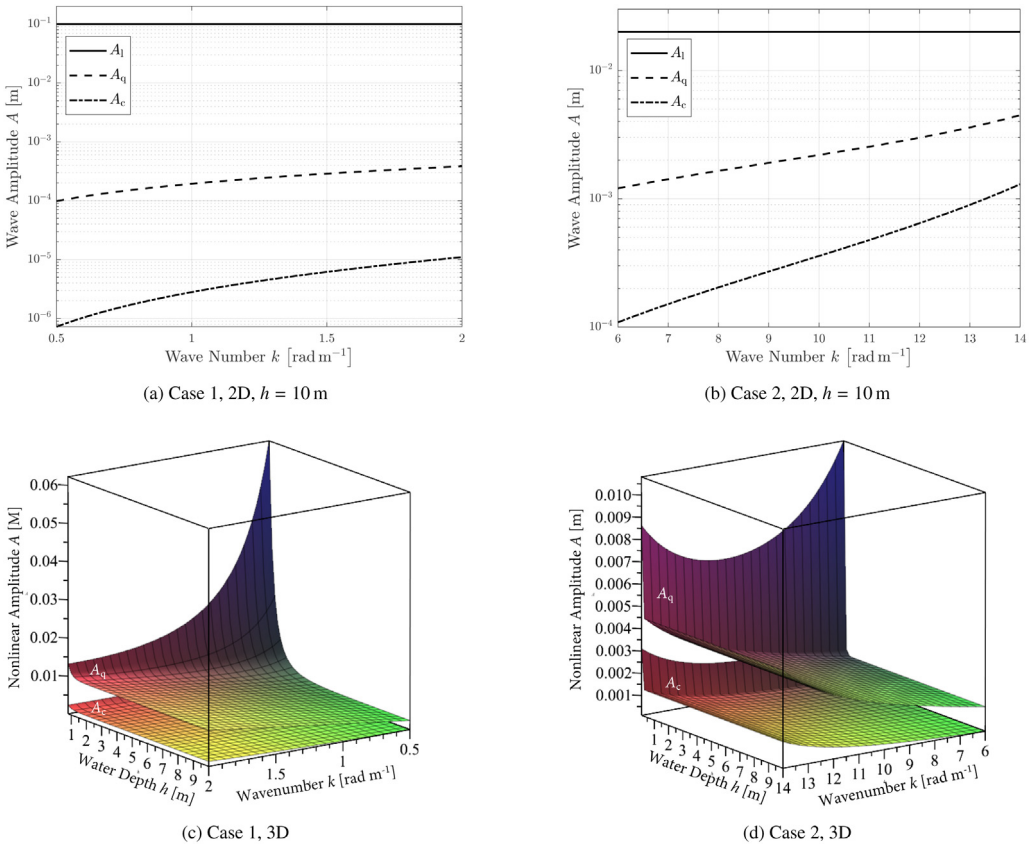

(a) Case 1, 2D, h = 10 m

(b) Case 2, 2D, h = 10 m

(c) Case 1, 3D

(d) Case 2, 3D

Fig. 5. Higher-order wave amplitudes varying with the h and k in Case 1 and Case 2. The first-order amplitudes, A_1, are set to 0.1 m and 0.02 m, consistent with Fig. 3. Ranges of k are roughly consistent with the characteristic values in literature.

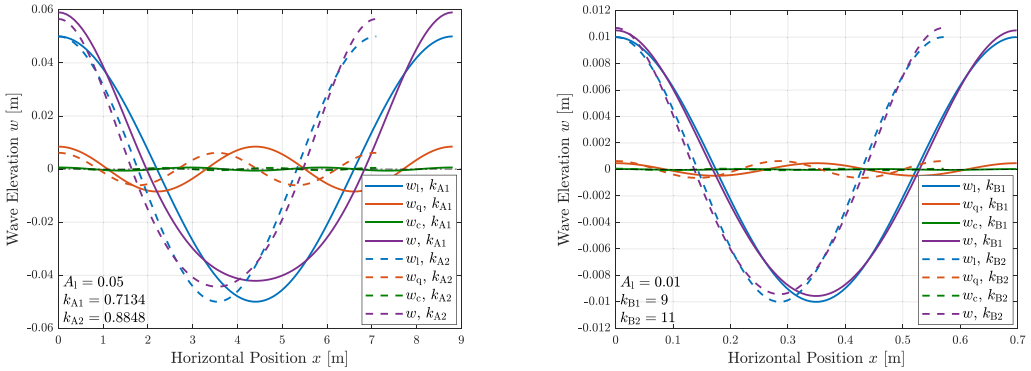

(a) Case 1

(b) Case 2

Fig. 6. Examples of wave form in Case 1 and Case 2. k is set for consistency with Section 4.2 and Fig. 6 in Ma et al. (2020) and Table 2 in Schreier and Jacobi (2020), respectively. A_1 is set in accordance with k to ensure $\varepsilon \approx 0.01$.

free surface position is taken into account in our model while it is not in Ma et al. (2020). Fig. 7(b) visualizes example waves generated by our solution and Ma et al. (2020), respectively. Our solution leads to weakly nonlinear phenomena as theoretically expected; Ma et al. (2020) leads to exaggerated nonlinear phenomena because of its singularity near $\omega \approx 2.08\,\mathrm{rad\,s^{-1}}$.

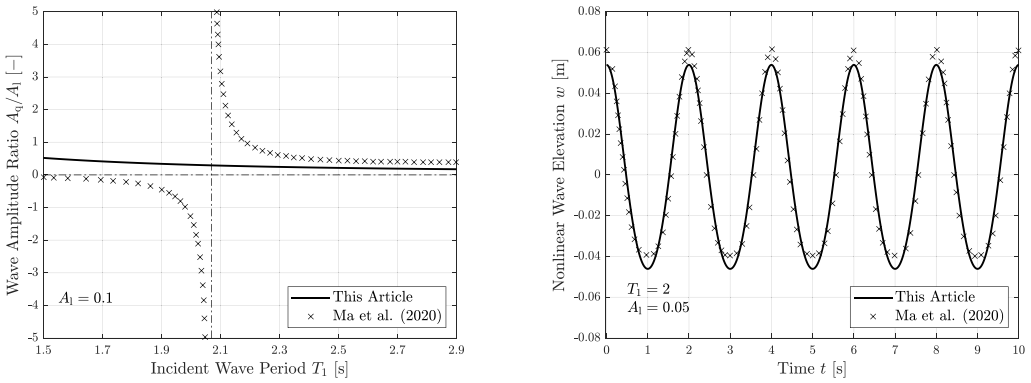

(a) Ratio of A_l/A_q (b) Time History

Fig. 7. Comparison with Ma et al. (2020) for Case 1. (a) is the comparison of $\frac{A_q}{A_l}$ with the incident wave amplitude 0.1 m, in which our results are calculated by Eqs. (41) and (51) of the present article and the published results are measured from Fig. 6 of the literature. (b) is the analogy of the nonlinear wave up to the second order between two analytical models with the incident wave amplitude 0.05 m, in which our results are calculated by Eqs. (41), (51) and (57) of the present article and the published results are measured from Fig. 5 of the literature.

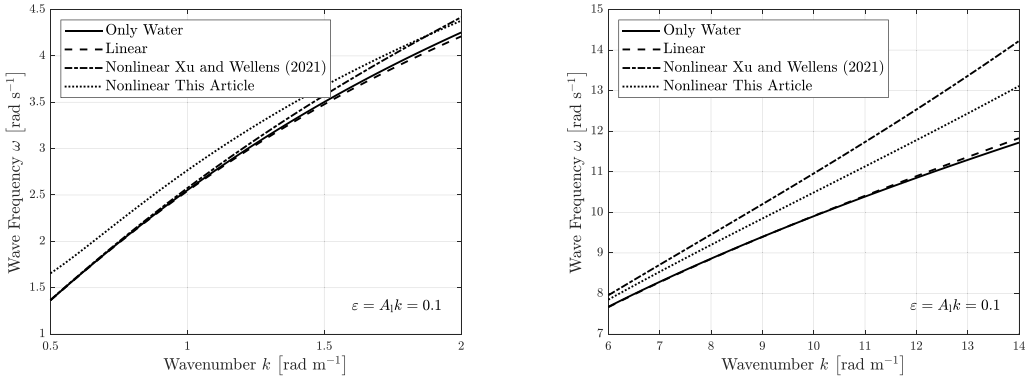

(a) Case 1 (b) Case 2

Fig. 8. Dispersion relations varying with wavenumber k in Case 1 and Case 2. The linear amplitudes are merged into the wave steepness to ensure $\varepsilon = 0.1$ in both Case 1 and Case 2. Other parameters are consistent to Table 2.

5.3. Dispersion relations

The dispersion relation relates the time domain (frequency) and the space domain (wavenumber). The derivation in Sections 4.1 and 4.2 shows that the dispersion relation does not feature quadratic terms. The hydroelastic dispersion relation is linear up to the second order (see Eq. (38)). The third-order nonlinearity leads to amplitude dispersion that is scaled by the wave steepness squared $\varepsilon^2 = A^2k^2$ (see Eq. (54)). Recall the amplitude dispersion relations in the EBVK theory for beam only and the Stokes theory for water waves only. In these two single-domain models, waves propagate faster with larger amplitudes; the increased celerity also is also scaled by the steepness squared. The consistency of nonlinearity verifies our solution that combines the third-order nonlinear EBVK beam and the third-order nonlinear Stokes wave, as stated in Table 1.

Fig. 8 illustrates dispersion relations in Case 1 and Case 2 under four conditions: only water, the linear FSI, the nonlinear FSI of nonlinear-structure-linear-water in Xu and Wellens (2021a), and the nonlinear FSI of nonlinear-structure-nonlinear-water in this article. The 2D visualization merges amplitudes into the wave steepness to ensure the perturbation $\varepsilon = 0.1$. The wavenumber range and other physical parameters are kept with Table 2.

The most obvious phenomenon is that the dispersion relation of the linear hydroelastics is close to that of only water wave in both Case 1 and Case 2. These results are determined by the chosen parameters and agree with the design objective of the articles where we took the physical parameters: the floating structure moves with the incident waves. The comparison between Figs. 8(a) and 8(b) indicates that the nonlinear effect is relatively small in Case 1, but large in Case 2. Fig. 8(a) indicates that the nonlinear effect on the dispersion relation is not significant. This can be explained by the fact that the plate-like structure in long waves does not deflect enough to show nonlinearity. Fig. 8(b) demonstrates

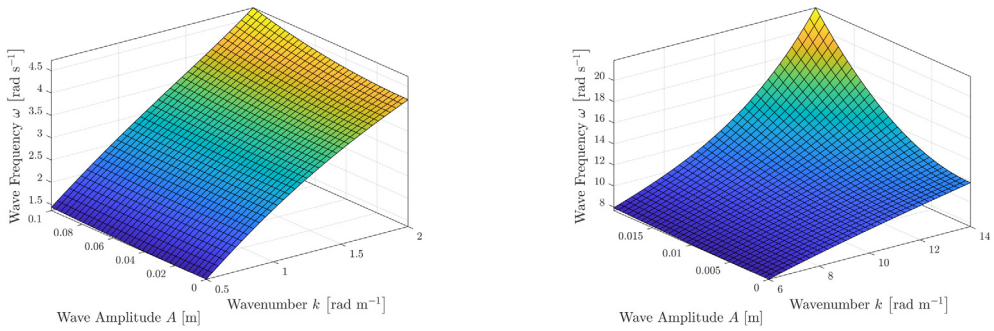

(a) Case 1 (b) Case 2

Fig. 9. Dispersion relations vary with wavenumber k and linear amplitude A_l in Case 1 and Case 2. The ranges of k are consistent with Table 2. The maximum of A_l is equivalent to characteristic values in Case 1 and Case 2, respectively.

that the membrane-like structure displays nonlinear behavior in the dispersion relation, with (this study) or without (Xu and Wellens, 2021a) nonlinear terms in the potential flow model for the fluid.

Fig. 9 provides 3D views of the frequency variation with both the wavenumber and amplitude. The maximum amplitude in Case 1 is consistent with the characteristic value in Section 4.2 and Fig. 6 of Ma et al. (2020); the maximum amplitude in Case 2 is consistent with the value in Table 2 of Schreier and Jacobi (2020). The wavenumber ranges are roughly equal to that in Table 2.

As physically expected, the wave frequency monotonically increases with both the wavenumber and wave amplitude, i.e., with the wave steepness. However, amplitude behaves differently between the pontoon- and the membrane-LFPV. The frequency increases fast with the amplitude in thin-film sheets (Case 2), whereas the increment is almost negligible in stiff plates (Case 1).

6. Conclusion

The present research considers the fully nonlinear FSI of LFPV with water beneath. It fills the gap between LFPV, which is a new application, and the model of ice sheets and VLFS, which is extensively discussed by academia. Considering the characteristics of LFPV, we propose to model LFPV by the nonlinear EBVK theory and water waves by the nonlinear Stokes theory. The fully analytical solution is derived up to the third order with the unified Stokes perturbation method. Building on the exact expressions of the analytical solution, the authors present the numerical values and compare them with two recent studies. One is the plate model suitable for pontoon LFPV, and the other is the membrane model that is suitable for membrane LFPV. The following remarks conclude our research:

- The nonlinear EBVK theory is suitable for LFPV, especially for the membrane-type structures. This EBVK model introduces the rotation-associated nonlinearity in the in-plane strain–stress relation, taking the nonlinearity due to the larger slope and the membrane force into account.
- The analytical solution unifies nonlinear paradigms in both the structural and the fluid domains. Hydroelastic waves are dominated by the linear property; wave peaks and troughs are respectively enhanced and reduced by the second-order nonlinearity; amplitude dispersion occurs in the third order term of the coupled system.
- Amplitude dispersion has a strong effect on the membrane-type LFPV, but almost no effect on the stiffer plate-type.
- Our theoretical model is especially suitable for membrane-type LFPV in all water depths. For the pontoon-type LFPV, the solution is valid in relatively deep waters.

The present article provides a theoretical nonlinear paradigm for analyzing the hydrodynamic properties of LFPV. Future research will be a systematic analysis of the singularity with very long waves and/or with very shallow waters.

CRediT authorship contribution statement

Pengpeng Xu: Conceptualization, Methodology, Software, Validation, Formal analysis, Investigation, Data curation, Writing – original draft, Writing – review & editing, Visualization. **Peter R. Wellens:** Conceptualization, Methodology, Software, Validation, Formal analysis, Investigation, Data curation, Writing – original draft, Writing – review & editing, Supervision.

Declaration of competing interest

The authors declare that they have no known competing financial interests or personal relationships that could have appeared to influence the work reported in this paper.

Acknowledgment

This research is financially supported by the program of China Scholarship Council (CSC) with project NO. 201707720039.

Appendix A

Considering the nonlinear EBVK beam and Airy wave, the nonlinear dynamic interface (free surface) boundary condition reads

$$\rho_s\delta\frac{\partial^2 w}{\partial t^2}+\frac{E\delta^3}{12\left(1-\nu^2\right)}\frac{\partial^4 w}{\partial x^4}-\frac{3}{2}E\delta\left(\frac{\partial w}{\partial x}\right)^2\frac{\partial^2 w}{\partial x^2}+\rho_{\mathrm{w}}\mathrm{g}w+\rho_{\mathrm{w}}\frac{\partial\phi}{\partial t}=0\quad\text{at}\quad z=0. \tag{A.1}$$

Other governing equations of the EBVK-Airy coupling system, namely the Laplace equation, the bottom condition, and the kinematic interface condition, are linear and thus omitted here.

Introduce normalized variables

$$\begin{cases} X=kx,\quad Z=kz,\quad \tau_{\mathrm{A}}=kt,\quad \varepsilon=Ak,\quad H=kh,\\ \kappa_{\mathrm{A}}=\dfrac{\delta^2k^2E}{12\left(1-\nu^2\right)\rho_s},\quad \alpha_{\mathrm{A}}=\dfrac{3E}{2\rho_s},\quad \beta_{\mathrm{A}}=\dfrac{\rho_{\mathrm{w}}\mathrm{g}}{\rho_s\delta k^2},\quad W=\dfrac{w}{A},\quad \Phi=\dfrac{k\phi}{A\mathrm{g}}. \end{cases} \tag{A.2}$$

With Eq. (A.2), Eq. (A.1) can be rewritten as

$$\frac{\partial^2 W}{\partial\tau_{\mathrm{A}}^2}+\kappa_{\mathrm{A}}\frac{\partial^4 W}{\partial X^4}+\beta_{\mathrm{A}}W+\beta_{\mathrm{A}}\frac{\partial\Phi}{\partial\tau_{\mathrm{A}}}-\varepsilon^2\alpha_{\mathrm{A}}\left(\frac{\partial W}{\partial X}\right)^2\frac{\partial^2 W}{\partial X^2}=0\quad\text{at}\quad Z=0. \tag{A.3}$$

Eq. (A.3) proves that the nonlinearity of the model that combines the nonlinear EBVK theory and linear potential theory is linear in the primary order. The nonlinearity stemming from the membrane force exists on a level that is twice higher than the primary hydroelastics. Therefore, it is third-order nonlinearity in the context of the present article.

Appendix B

$$c_1=\beta\cosh(2kh)+2k\sinh(2kh) \tag{B.1}$$

$$c_2=32\kappa k^5\sinh(2kh)+2\beta\mathrm{g}k\sinh(2kh) \tag{B.2}$$

$$c_3=\frac{\omega_1\left(\beta\cosh^2(kh)\,\omega_1^2-\frac{k}{2}\sinh(2kh)\left(16k^4\kappa+\beta\mathrm{g}-4\omega_1^2\right)-\frac{3\beta\omega_1^2}{2}\right)}{\sinh^2(kh)\cos(2kx)} \tag{B.3}$$

$$c_4=\frac{16k\sinh(2kh)\,\omega_1\left(k^4\kappa-\frac{\omega_1^2}{4}+\frac{\beta\mathrm{g}}{16}\right)-\beta\omega_1^3\left(\cosh(2kh)-2\right)}{\cos(2kx)\left(\cosh(2kh)-1\right)\left(4\left(\beta\cosh(2kh)+2k\sinh(2kh)\,\omega_1^2\right)-32k^5\kappa\sinh(2kh)-2k\beta\mathrm{g}\sinh(2kh)\right)} \tag{B.4}$$

$$c_5=\frac{16k\sinh(2kh)\,\omega_1\left(k^4\kappa-\frac{\omega_1^2}{4}+\frac{\beta\mathrm{g}}{16}\right)-\beta\omega_1^3\left(\cosh(2kh)-2\right)}{\left(\cosh(2kh)-1\right)\left(4\left(\beta\cosh(2kh)+2k\sinh(2kh)\,\omega_1^2\right)-32k^5\kappa\sinh(2kh)-2k\beta\mathrm{g}\sinh(2kh)\right)} \tag{B.5}$$

$$c_6=\frac{\beta k\omega_1^2\cosh(kh)\left(\cosh^2(kh)+\frac{1}{2}\right)}{2\sinh(kh)\left(2\beta\omega_1^2\cosh^2(kh)+k\sinh(kh)\cosh(kh)\left(4\omega_1^2-\beta\mathrm{g}-16k^4\kappa\right)-\beta\omega_1^2\right)} \tag{B.6}$$

$$\begin{aligned} c_7=&\cosh^5(kh)\left(\left(-2\alpha\kappa-\frac{13}{3}\kappa^2\beta^2\right)k^8-\frac{7}{3}\alpha\beta^2\kappa k^6-\frac{11}{3}\left(\beta^2\kappa-\frac{3}{22}\alpha\right)\mathrm{g}\beta k^4+\frac{1}{6}\alpha\beta^3\mathrm{g}k^2+\frac{2}{3}\beta^4\mathrm{g}^2\right)\\ &+\cosh^4(kh)\sinh(kh)\,\beta\kappa\left(-\frac{13}{3}\alpha\kappa k^6-3\beta\mathrm{g}\kappa k^4+\frac{2}{3}\alpha\beta\mathrm{g}k^2-4\kappa^2k^8+\beta^2\mathrm{g}^2\right)\\ &+\cosh^3\left(\left(4\alpha\kappa+\frac{28}{3}\beta^2\kappa^2\right)k^8+\frac{13}{6}\alpha\beta^2\kappa k^6+\frac{26}{3}\beta\mathrm{g}\left(\beta^2\kappa-\frac{3}{26}\alpha\right)k^4-\frac{1}{3}\alpha\beta^3\mathrm{g}k^2-\frac{2}{3}\beta^4\mathrm{g}^2\right)\\ &-2\cosh^2(kh)\sinh(kh)\,\beta k\left(-4\kappa^2k^8-\frac{25}{12}\alpha\kappa k^6-3\beta\kappa\mathrm{g}k^4+\frac{5}{12}\alpha\beta\mathrm{g}k^2+\beta^2\mathrm{g}^2\right)\\ &+\cosh\left(\left(\frac{3}{4}\beta^2\kappa^2-2\alpha\kappa\right)k^8+\frac{1}{6}\alpha\beta^2\kappa k^6+\frac{3}{2}\left(\beta^2\kappa+\frac{\alpha}{3}\right)\mathrm{g}\beta k^4+\frac{1}{6}\alpha\beta^3\mathrm{g}k^2+\frac{3}{4}\beta^4\mathrm{g}^2\right)\\ &+\frac{1}{6}\sinh(kh)\,\alpha\beta k^3\left(\kappa k^4+\beta\mathrm{g}\right) \end{aligned} \tag{B.7}$$

$$
\begin{aligned}
c_8 =& 4\sinh^2(kh)\left(\kappa k^4+\beta g\right)\left(\cosh^3(kh)\left(-4\kappa k^6-\frac{14}{3}\beta^2\kappa k^4+\beta g k^2+\frac{1}{3}\beta^3 g\right)\right.\\
&+\frac{4}{3}\cosh^2(kh)\sinh(kh)\,\kappa\beta\left(-\frac{13}{2}\kappa k^4+\beta g\right)\\
&+\cosh(kh)\left(4\kappa k^6-\frac{1}{3}\beta^2\kappa k^4-\beta g k^2-\frac{1}{3}\beta^3 g\right)\\
&\left.-\frac{1}{3}\sinh(kh)\,\beta k\left(\kappa k^4+\beta g\right)\right)
\end{aligned}
\tag{B.8}
$$

$$
\begin{aligned}
c_9 =& \cosh^5(kh)\left(-11664k^{10}\kappa^2-96\alpha k^8\kappa-9\kappa\left(97\beta g-468\omega_1^2\right)k^6-6\alpha\left(\beta g-4\omega_1^2\right)k^4\right.\\
&\left.-9\left(\beta g-4\omega_1^2\right)\left(\beta g-9\omega_1^2\right)k^2-12\beta^2\omega_1^4\right)\\
&+\cosh^4(kh)\sinh(kh)\,\beta k\omega_1^2\left(336k^4\kappa+12\alpha k^2+21\beta g-84\omega_1^2\right)\\
&+6\cosh^3(kh)\left(2592k^{10}\kappa+32\alpha k^8\kappa+2\left(97\beta g\kappa-468\kappa\omega_1^2\right)k^6+2\alpha\left(\beta g-4\omega_1^2\right)k^4\right.\\
&\left.2\left(\beta^2 g^2-13\beta g\omega_1^2+36\omega_1^2\right)k^2+9\beta^2\omega_1^4\right)\\
&-45\cosh^2(kh)\sinh(kh)\,k\beta\omega_1^2\left(42k^4\kappa+\frac{2}{5}\alpha k^2+\beta g-6\omega_1^2\right)\\
&-3\cosh(kh)\left(1296k^{10}\kappa^2+32\alpha k^8\kappa+\left(97\beta g\kappa-468\kappa\omega_1^2\right)k^6+2\alpha\left(\beta g-4{\omega_1}^2\right)k^4\right.\\
&\left.+\left(\beta^2 g^2-13\beta g{\omega_1}^2+36{\omega_1}^4\right)k^2+15\beta^2\omega_1^4\right)\\
&+6\sinh(kh)\,\beta k\omega_1^2\left(81k^4\kappa+\alpha k^2+\beta g-9\omega_1^2\right)
\end{aligned}
\tag{B.9}
$$

$$
\begin{aligned}
c_{10} =& \frac{1}{8\left(-2\beta\cosh^2(kh)\,\omega_1^2+\sinh(kh)\,k\left(16k^4\kappa+\beta g-4\omega_1^2\right)\cosh(kh)+\beta\omega_1^2\right)}\\
&\cdot\frac{1}{\sinh^3(kh)}\cdot\frac{k\omega_1\cosh(3k(z+h))}{3k\left(\beta g-9\omega_1^2+81\kappa\right)\sinh(3k(z+h))-9\cosh(3k(z+h))\,\beta\omega_1^2}
\end{aligned}
\tag{B.10}
$$

$$
\begin{aligned}
c_{11} =& -\frac{9}{4}\cosh^3(kh)\,k^3\sinh(kh)\left(16k^4\kappa+\beta g-4\omega_1^2\right)-\frac{9}{2}k^2\cosh^2(kh)\,\beta\omega_1^2\\
&+\frac{3}{4}\cosh(kh)\sinh(kh)\,k^3\left(16k^4\kappa+\beta g-4\omega_1^2\right)+\frac{3}{2}k^2\beta\omega_1^2
\end{aligned}
\tag{B.11}
$$

$$
c_{12} = -12\beta\omega_1^2\cosh^2(kh)+6k\left(16k^4\kappa+\beta g-4\omega_1^2\right)\sinh(kh)\cosh(kh)+6\beta\omega_1^2 \tag{B.12}
$$

References

Andrianov, A.I., Hermans, A.J., 2003. The influence of water depth on the hydroelastic response of a very large floating platform. Mar. Struct. 16 (5), 355–371. http://dx.doi.org/10.1016/S0951-8339(03)00023-6.

Andrianov, A., Hermans, A., 2005. Hydroelasticity of a circular plate on water of finite or infinite depth. J. Fluids Struct. 20 (5), 719–733. http://dx.doi.org/10.1016/j.jfluidstructs.2005.03.002.

Balmforth, N.J., Craster, R.V., 1999. Ocean waves and ice sheets. J. Fluid Mech. 395, 89–124. http://dx.doi.org/10.1017/S0022112099005145.

Batyaev, E.A., Khabakhpasheva, T.I., 2015. Hydroelastic waves in a channel covered with a free ice sheet. Fluid Dyn. 50 (6), 775–788. http://dx.doi.org/10.1134/S0015462815060071.

Bjørneklett, B., 2018. Offshore floating solar – a technical perspective. PV Tech. Power 16, 60–63, URL: https://www.pv-tech.org/technical-papers/offshore-floating-solar-a-technical-perspective/.

Cazzaniga, R., Cicu, M., Rosa-Clot, M., Rosa-Clot, P., Tina, G.M., Ventura, C., 2018. Floating photovoltaic plants: Performance analysis and design solutions. Renew. Sustain. Energy Rev. 81, 1730–1741. http://dx.doi.org/10.1016/j.rser.2017.05.269.

Chen, X.J., Jensen, J.J., Cui, W.C., Fu, S.X., 2003a. Hydroelasticity of a floating plate in multidirectional waves. Ocean Eng. 30 (15), 1997–2017. http://dx.doi.org/10.1016/S0029-8018(03)00020-9.

Chen, X., Wu, Y., Cui, W., Tang, X., 2003b. Nonlinear hydroelastic analysis of a moored floating body. Ocean Eng. 30 (8), 965–1003. http://dx.doi.org/10.1016/S0029-8018(02)00078-1.

Cheng, Y., Ji, C., Zhai, G., Gaidai, O., 2016a. Hydroelastic analysis of oblique irregular waves with a pontoon-type VLFS edged with dual inclined perforated plates. Mar. Struct. 49, 31–57. http://dx.doi.org/10.1016/j.marstruc.2016.05.008.

Cheng, Y., Ji, C., Zhai, G., Oleg, G., 2016b. Dual inclined perforated anti-motion plates for mitigating hydroelastic response of a VLFS under wave action. Ocean Eng. 121, 572–591. http://dx.doi.org/10.1016/j.oceaneng.2016.05.044.

Cheng, Y., Ji, C., Zhai, G., Oleg, G., 2017. Fully nonlinear numerical investigation on hydroelastic responses of floating elastic plate over variable depth sea-bottom. Mar. Struct. 55, 37–61. http://dx.doi.org/10.1016/j.marstruc.2017.04.005.

Cheng, Y., Zhai, G.-j., Ou, J., 2014. Time-domain numerical and experimental analysis of hydroelastic response of a very large floating structure edged with a pair of submerged horizontal plates. Mar. Struct. 39, 198–224. http://dx.doi.org/10.1016/j.marstruc.2014.07.007.

Dingemans, M.W., 1997. Water Wave Propagation over Uneven Bottoms, Vol. 13. World Scientific.

Fenton, J.D., 1999. Numerical methods for nonlinear waves. In: Advances in Coastal and Ocean Engineering, vol. 5, WORLD SCIENTIFIC, pp. 241–324. http://dx.doi.org/10.1142/9789812797544_0005.

Fenton, J.D., McKee, W.D., 1990. On calculating the lengths of water waves. Coast. Eng. 14 (6), 499–513. http://dx.doi.org/10.1016/0378-3839(90)90032-R.
Forbes, L.K., 1986. Surface waves of large amplitude beneath an elastic sheet. Part 1. high-order series solution. J. Fluid Mech. 169, 409–428. http://dx.doi.org/10.1017/S0022112086000708.
Forbes, L.K., 1988. Surface waves of large amplitude beneath an elastic sheet. Part 2. Galerkin solution. J. Fluid Mech. 188, 491–508. http://dx.doi.org/10.1017/S0022112088000813.
Gorjian, S., Sharon, H., Ebadi, H., Kant, K., Scavo, F.B., Tina, G.M., 2021. Recent technical advancements, economics and environmental impacts of floating photovoltaic solar energy conversion systems. J. Cleaner Prod. 278, 124285. http://dx.doi.org/10.1016/j.jclepro.2020.124285.
Hegarty, G.M., Squire, V.A., 2008. A boundary-integral method for the interaction of large-amplitude ocean waves with a compliant floating raft such as a sea-ice floe. J. Eng. Math. 62 (4), 355–372. http://dx.doi.org/10.1007/s10665-008-9219-1.
Holthuijsen, L.H., 2007. Waves in Oceanic and Coastal Waters. Cambridge University Press, Cambridge, http://dx.doi.org/10.1017/CBO9780511618536.
Iijima, K., Fujikubo, M., 2018. Hydro-elastoplastic behaviour of VLFS under extreme vertical bending moment by segmented beam approach. Mar. Struct. 57, 1–17. http://dx.doi.org/10.1016/j.marstruc.2017.09.008.
Iijima, K., Fujikubo, M., 2019. Analytical formula for collapse extent of VLFS under extreme vertical bending moment. J. Mar. Sci. Technol. 24 (2), 372–381. http://dx.doi.org/10.1007/s00773-018-0555-1.
Ikhennicheu, M., Danglade, B., Pascal, R., Arramounet, V., Trébaol, Q., Gorintin, F., 2021. Analytical method for loads determination on floating solar farms in three typical environments. Sol. Energy 219, 34–41. http://dx.doi.org/10.1016/j.solener.2020.11.078.
Ilyas, M., Meylan, M.H., Lamichhane, B., Bennetts, L.G., 2018. Time-domain and modal response of ice shelves to wave forcing using the finite element method. J. Fluids Struct. 80, 113–131. http://dx.doi.org/10.1016/j.jfluidstructs.2018.03.010.
Kagemoto, H., Fujino, M., Murai, M., 1998. Theoretical and experimental predictions of the hydroelastic response of a very large floating structure in waves. Appl. Ocean Res. 20 (3), 135–144. http://dx.doi.org/10.1016/S0141-1187(98)00017-0.
Kagemoto, H., Fujino, M., Zhu, T., 1997. On the estimation method of hydrodynamic forces acting on a very large floating structure. Appl. Ocean Res. 19 (1), 49–60. http://dx.doi.org/10.1016/S0141-1187(97)00009-6.
Karperaki, A.E., Belibassakis, K.A., 2021a. Hydroelastic analysis of very large floating structures in variable bathymetry regions by multi-modal expansions and FEM. J. Fluids Struct. 102, 103236. http://dx.doi.org/10.1016/j.jfluidstructs.2021.103236.
Karperaki, A.E., Belibassakis, K.A., 2021b. Hydroelastic analysis of very large floating structures in variable bathymetry regions by multi-modal expansions and FEM. J. Fluids Struct. 102, 103236. http://dx.doi.org/10.1016/j.jfluidstructs.2021.103236.
Kumar, M., Kumar, A., 2020. Experimental characterization of the performance of different photovoltaic technologies on water bodies. Prog. Photovolt., Res. Appl. 28 (1), 25–48. http://dx.doi.org/10.1002/pip.3204.
Lamas-Pardo, M., Iglesias, G., Carral, L., 2015. A review of very large floating structures (VLFS) for coastal and offshore uses. Ocean Eng. 109, 677–690. http://dx.doi.org/10.1016/j.oceaneng.2015.09.012.
Levi-Civita, T., 1925. Détermination rigoureuse des ondes permanentes d'ampleur finie. Math. Ann. 93 (1), 264–314. http://dx.doi.org/10.1007/BF01449965.
Liu, X., Wang, X., Xu, S., 2020. A DMM-EMM-RSM hybrid technique on two-dimensional frequency-domain hydroelasticity of floating structures over variable bathymetry. Ocean Eng. 201, 107135. http://dx.doi.org/10.1016/j.oceaneng.2020.107135.
Ma, C., Iijima, K., Oka, M., 2020. Nonlinear waves in a floating thin elastic plate, predicted by a coupled SPH and FEM simulation and by an analytical solution. Ocean Eng. 204, 107243. http://dx.doi.org/10.1016/j.oceaneng.2020.107243.
Newman, J.N., 1994. Wave effects on deformable bodies. Appl. Ocean Res. 16 (1), 47–59. http://dx.doi.org/10.1016/0141-1187(94)90013-2.
Ocean Sun, 2021. Ocean sun projects. URL: https://oceansun.no/projects/. (Accessed 2021 March 18).
Oliveira-Pinto, S., Stokkermans, J., 2020. Assessment of the potential of different floating solar technologies – overview and analysis of different case studies. Energy Convers. Manage. 211, 112747. http://dx.doi.org/10.1016/j.enconman.2020.112747.
Părău, E., Dias, F., 2002. Nonlinear effects in the response of a floating ice plate to a moving load. J. Fluid Mech. 460, 281–305. http://dx.doi.org/10.1017/S0022112002008236.
Patil Desai Sujay, S., Wagh, M., Shinde, N., 2017. A review on floating solar photovoltaic power plants. Int. J. Sci. Eng. Res. 8 (6), 789.
Peake, N., 2001. Nonlinear stability of a fluid-loaded elastic plate with mean flow. J. Fluid Mech. 434, 101–118. http://dx.doi.org/10.1017/s0022112001003573.
Porter, R., 2019. The coupling between ocean waves and rectangular ice sheets. J. Fluids Struct. 84, 171–181. http://dx.doi.org/10.1016/j.jfluidstructs.2018.09.004.
Pringle, A., Handler, R., Pearce, J., 2017. Aquavoltaics: Synergies for dual use of water area for solar photovoltaic electricity generation and aquaculture. Renew. Sustain. Energy Rev. 80, 572–584. http://dx.doi.org/10.1016/j.rser.2017.05.191.
Ren, N., Zhang, C., Magee, A.R., Hellan, Ø., Dai, J., Ang, K.K., 2019. Hydrodynamic analysis of a modular multi-purpose floating structure system with different outermost connector types. Ocean Eng. 176, 158–168. http://dx.doi.org/10.1016/j.oceaneng.2019.02.052.
Riyansyah, M., Wang, C.M., Choo, Y.S., 2010. Connection design for two-floating beam system for minimum hydroelastic response. Mar. Struct. 23 (1), 67–87. http://dx.doi.org/10.1016/j.marstruc.2010.01.001.
Rosa-Clot, M., Tina, G.M., 2018. Submerged PV systems. In: Submerged and Floating Photovoltaic Systems. Academic Press, pp. 65–87. http://dx.doi.org/10.1016/B978-0-12-812149-8.00004-1, chapter 4.
Sahu, A., Yadav, N., Sudhakar, K., 2016. Floating photovoltaic power plant: A review. Renew. Sustain. Energy Rev. 66, 815–824. http://dx.doi.org/10.1016/j.rser.2016.08.051.
Schreier, S., Jacobi, G., 2020. Experimental investigation of wave interaction with a thin floating sheet. In: Proceedings of the International Offshore and Polar Engineering Conference, 2020-October, pp. 2479–2488, ISOPE-I-20-3238.
Schwartz, L.W., 1974. Computer extension and analytic continuation of Stokes' expansion for gravity waves. J. Fluid Mech. 62 (3), 553–578. http://dx.doi.org/10.1017/S0022112074000802.
Soukissian, T.H., Karathanasi, F.E., Zaragkas, D.K., 2021. Exploiting offshore wind and solar resources in the mediterranean using ERA5 reanalysis data. Energy Convers. Manage. 237, 114092. http://dx.doi.org/10.1016/j.enconman.2021.114092.
Squire, V., Hosking, R.J., Kerr, A.D., Langhorne, P., 1996. Moving Loads on Ice Plates, Vol. 45. Springer Netherlands, http://dx.doi.org/10.1007/978-94-009-1649-4.
Stokes, G.G., 2009. On the theory of oscillatory waves. In: Mathematical and Physical Papers. In: Cambridge Library Collection - Mathematics, vol. 1, Cambridge University Press, pp. 197–229. http://dx.doi.org/10.1017/CBO9780511702242.013.
Strathdee, J., Robinson, W.H., Haines, E.M., 1991. Moving loads on ice plates of finite thickness. J. Fluid Mech. 226, 37–61. http://dx.doi.org/10.1017/s0022112091002288.
Struik, D., 1926. Détermination rigoureuse des ondes irrotationelles périodiques dans un canal à profondeur finie. Math. Ann. 95, 595–634.
Suzuki, H., Harada, H., Natsume, T., Maeda, K., Iijima, K., Hayashi, T., 2017. Technical challenge on VLFS in Japan after mega-float project. In: ASME 2017 36th International Conference on Ocean, Offshore and Arctic Engineering, Vol. 9. Trondheim, Norway, http://dx.doi.org/10.1115/omae2017-62663.

Suzuki, H., Riggs, H.R., Fujikubo, M., Shugar, T.A., Seto, H., Yasuzawa, Y., Bhattacharya, B., Hudson, D.A., Shin, H., 2006. Very large floating structures. In: ASME 2007 26th International Conference on Offshore Mechanics and Arctic Engineering, Volume 2: Structures, Safety and Reliability; Petroleum Technology Symposium. pp. 597–608. http://dx.doi.org/10.1115/omae2007-29758.

Trapani, K., Millar, D.L., 2014. The thin film flexible floating PV (T3F-PV) array: The concept and development of the prototype. Renew. Energy 71, 43–50. http://dx.doi.org/10.1016/j.renene.2014.05.007.

Trapani, K., Millar, D.L., Smith, H.C., 2013. Novel offshore application of photovoltaics in comparison to conventional marine renewable energy technologies. Renew. Energy 50, 879–888. http://dx.doi.org/10.1016/j.renene.2012.08.043.

Trapani, K., Redón Santafé, M., 2015. A review of floating photovoltaic installations: 2007–2013. Prog. Photovolt., Res. Appl. 23 (4), 524–532. http://dx.doi.org/10.1002/pip.2466.

Ursell, F., 1953. The long-wave paradox in the theory of gravity waves. Math. Proc. Camb. Phil. Soc. 49 (4), 685–694. http://dx.doi.org/10.1017/S0305004100028887.

Vanden-Broeck, J.-M., Părău, E.I., 2011. Two-dimensional generalized solitary waves and periodic waves under an ice sheet. Phil. Trans. R. Soc. A 369 (1947), 2957–2972. http://dx.doi.org/10.1098/rsta.2011.0108.

Wang, C.D., Meylan, M.H., 2002. The linear wave response of a floating thin plate on water of variable depth. Appl. Ocean Res. 24 (3), 163–174. http://dx.doi.org/10.1016/S0141-1187(02)00025-1.

World Bank Group, Energy Sector Management Assistance Program, Solar Energy Research Institute of Singapore, 2019. Where sun meets water : Floating solar market report. URL: https://openknowledge.worldbank.org/handle/10986/31880, ©, World Bank.

Xu, P., Wellens, P.R., 2021a. Theoretical analysis of fully nonlinear fluid-structure interaction between large-scale polymer offshore floating photovoltaics and water waves. A Journal, Manuscript (submitted for publication).

Xu, P., Wellens, P., 2021b. Effects of static loads on the nonlinear vibration of circular plates. J. Sound Vib. 504, 116111. http://dx.doi.org/10.1016/j.jsv.2021.116111.

Yang, J.S., 2017. Hybrid active and passive control of a very large floating beam structure. Nonlinear Dynam. 87 (3), 1835–1845. http://dx.doi.org/10.1007/s11071-016-3156-8.

Zhang, H., Xu, D., Lu, C., Qi, E., Hu, J., Wu, Y., 2015a. Amplitude death of a multi-module floating airport. Nonlinear Dynam. 79 (4), 2385–2394. http://dx.doi.org/10.1007/s11071-014-1819-x.

Zhang, H., Xu, D., Xia, S., Lu, C., Qi, E., Tian, C., Wu, Y., 2015b. Nonlinear network modeling of multi-module floating structures with arbitrary flexible connections. J. Fluids Struct. 59, 270–284. http://dx.doi.org/10.1016/j.jfluidstructs.2015.09.012.

Zhang, H., Xu, D., Xia, S., Wu, Y., 2018. Nonlinear dynamics of a non-autonomous network with coupled discrete–continuum oscillators. Nonlinear Dynam. 94 (2), 889–904. http://dx.doi.org/10.1007/s11071-018-4400-1.